aerospace

MDPI

Article

Dust Ingestion in a Rotorcraft Engine Compressor: Experimental and Numerical Study of the Fouling Rate

Alessandro Vulpio *, Alessio Suman, Nicola Casari and Michele Pinelli

Department of Engineering (DE), University of Ferrara, Via Giuseppe Saragat 1, 44122 Ferrara, Italy; alessio.suman@unife.it (A.S.); nicola.casari@unife.it (N.C.); michele.pinelli@unife.it (M.P.)
* Correspondence: alessandro.vulpio@unife.it; Tel.: +39-0532-974-964

Abstract: Helicopters often operate in dusty sites, ingesting huge amounts of contaminants during landing, take-off, hover-taxi, and ground operations. In specific locations, the downwash of the rotor may spread soil particles from the ground into the environment and, once ingested by the engine, may stick to the compressor airfoils. In the present work, the Allison 250 C18 engine's multistage axial-flow compressor is employed to study the fouling rate on rotor blades and stator vanes from both numerical and experimental standpoints. The compressor is operated in a typical ground-idle operation, in terms of the rotational regime and contaminant concentration, in laboratory-controlled conditions. The mass of deposits is collected from the airfoil surfaces at the end of the test and compared to that estimated through the numerical model. The experimental test shows that the airfoils collect almost 1.6% of the engine's total mass ingested during a ground-idle operation. The capability of numerical methods to predict the fouling rate on the rotating and stationary airfoils of a multistage compressor is tested through the implementation of literature based deposition models. Sticking models show a good agreement in terms of the relative results; nevertheless, an overestimation of the deposited mass predicted is observed.

Keywords: fouling; deposition modeling; compressor degradation; rotorcraft; ground operation

Citation: Vulpio, A.; Suman, A.; Casari, N.; Pinelli M. Dust Ingestion in a Rotorcraft Engine Compressor: Experimental and Numerical Study of the Fouling Rate. *Aerospace* **2021**, *8*, 81. https://doi.org/10.3390/aerospace8030081

Academic Editor: Christian Breitsamter

Received: 26 February 2021
Accepted: 13 March 2021
Published: 18 March 2021

1. Introduction

Helicopter employment in civil and military operations is widespread and often essential for critical tasks such as search and rescue missions, firefighting, or medical evacuations. Landing and take-off operations from rugged and harsh sites make these kinds of maneuvers extremely complex and affected by low margins of error. Lands characterized by dusty floor conditions or poorly aggregated soil (such as arid locations and deserts) are considered the worst scenarios for helicopter operations to be successfully carried out [1]. In such locations, dust cloud raising events (named brownouts) are extremely likely and potentially harmful for the helicopter's operability. In the worst case of hard brownouts, pilots can incur diminished (or even zeroed) visibility conditions, which can pose an immediate threat to the safety of the aircraft [2].

Nevertheless, the occurrence of brownout events may expose the engine to a severe dust particle ingestion, leading to the deterioration of the internal components and the consequent reduction of the engine performance [3]. The compressor deterioration caused by the material removal (erosion) was documented for the first time during the U.S. Army's rotorcraft operations in Southeast Asia (during the 1960s) [4] and has been mitigated through the implementation of cyclone separator systems (i.e., Donaldson strata-tube^{TM}) capable of avoiding the entering of coarser particle into the engine flow path [5]. Despite this, the finest dust particles (below 5 μm) are allowed to enter the engine, due to the absence of separators, and deposit onto the compressor airfoils (fouling) [6]. The macroscopic effects of micro-sized solid particle adhesion are the decrease in the engine shaft power at constant turbine inlet temperature, the increase in the specific fuel consumption at constant

power, the decrease in the engine surge margin, and the reduced transient stability of the engine [7].

During take-off, landing, and hover-taxi operations, the engine may ingest huge amounts of dust, and a portion of that adheres to the compressor airfoils. For example, the downwash of the rotor wings increases dust concentration up to 10 m in altitude during operations in dusty areas. Figure 1a reports a series of dust concentration measurements over altitude on six rotorcraft frames performing hover maneuvers in the Yuma Proving Ground (Arizona) [8]. The measurements show that the dust concentration can increase up to 2500 mg/m^3 at ground level, depending on the rotorcraft frame weight, and spread up to seven meters in altitude.

During take-off operations, the aircraft can be exposed to dust ingestion for an extended time, even after the ground has been left. This fact is connected to the profile (take-off corridor) that a helicopter has to follow starting from the ground at zero airspeed (speed of the aircraft relative to the air). The height-velocity diagram indicates the combinations of altitude and velocity that should be avoided to ensure a safe emergency landing in case of power or transmission failure. This chart has been often referred to by the quaint name of the dead man's curve. A qualitative reproduction of the Sikorsky S-76 height-velocity chart is reported in Figure 1b. The chart reports the recommended profile that a pilot should follow before starting the cruise, and as can be noted, the helicopter should keep a low altitude until an optimal airspeed is reached, making the occurrence of dust ingestion more likely.

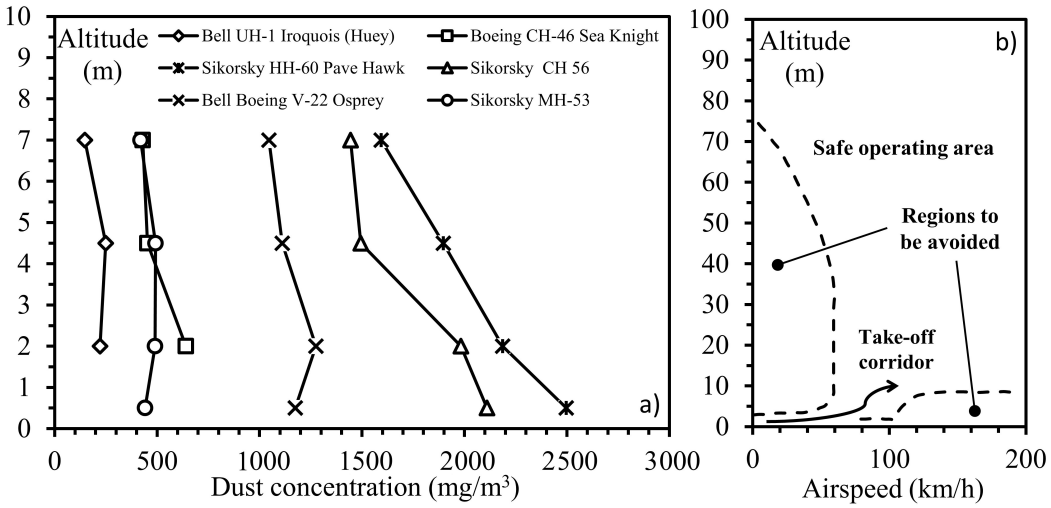

Figure 1. Operative conditions of a rotorcraft: (**a**) dust concentration profiles over altitude for six helicopter frames [8]; and (**b**) qualitative reproduction of the height-velocity curve of the Sikorsky S-76 helicopter, adapted from [9].

In order to give further information about the dangerousness of aircraft engine exposure to dusty environments, Clarkson et al. [10] introduced the concept of the dose of dust ingestion, which is the product of the particle concentration into the environment (C) and the exposure time (t) of the engine to that environment. This parameter allows completing the framework of the potential damage related to dust ingestion, which was, before 2010 (when the airspace over Europe was closed due to the volcanic ash emergency), based only on dust concentration limits, generally from 2 mg/m^3 to 6 mg/m^3 [11]. The scientific community has accepted the concept of dose and employed it in modeling deposition phenomena in aircraft engines [12,13]. In [10], the authors related the intensity of the aircraft damages (based on a historical survey) to the dust concentration encountered by the engine, and they proposed a safe-to-fly chart, which resumes the engine potential safety implications. A qualitative reproduction of the safe-to-fly chart is depicted in Figure 2, showing regions of safe operation, potential long-term damage operation, dangerous operation, and unsafe operation. Despite this chart is explicitly obtained for crashes caused

by ash plume ingestion, it can be used to explore the operative ranges where rotorcraft ground operations are located. Due to the high concentration encountered potentially in near-ground operations [8] and the relatively short time required for these maneuvers to be completed, it seems reasonable to locate the working conditions in the bottom right zone of the chart. A dashed rectangle is superimposed on the region of interest in Figure 2. As can be noted, these operative conditions overpass the safe-to-fly dose limit (generally assumed equal to 14.4 gs/m^3). Repeated cycles in such conditions may bring a progressive accumulation of dust particles and a reduction of the engine performance over time [14].

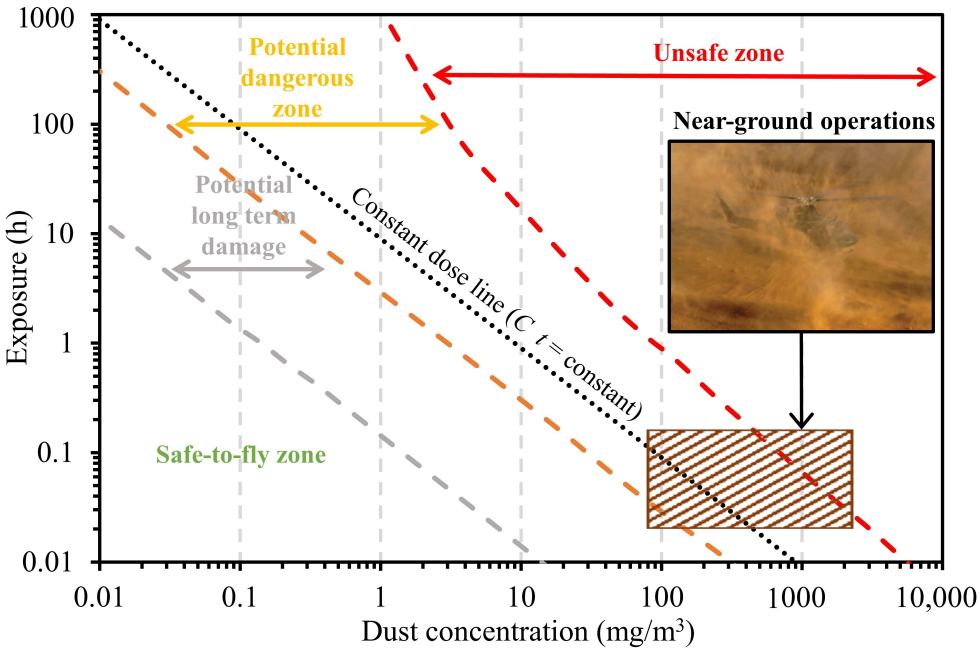

Figure 2. Safe-to-fly chart reporting the regions of safe operation, potential long-term damage operation, dangerous operation, and unsafe operation (adapted from [10]). The dashed rectangle reports the typical ground and near-ground conditions encountered by a rotorcraft in dusty sites.

The interest in compressor fouling study is twofold: (i) from the maintenance point of view, the prediction of the amount of deposited mass over the gas turbine's operative life can help to schedule and optimize overhaul and washing operations [15], leading to a significant reduction of costs; while (ii) from the component design standpoint, a more robust approach may be introduced to minimize the losses derived from fouling [16]. Experimental and numerical techniques have been employed to reproduce and understand the complex phenomena underlying the particle adhesion on compressor blades and vanes. Experimental works employed mainly cascades [17] or simplified profiles [18,19], while numerical approaches employed Lagrangian tracking techniques in CFD codes to reproduce the particle motion. The multi-phase scheme is coupled with sticking models to reproduce the adhesion phenomena [20,21].

In the present work, both experimental and numerical methods were used to gain insight into understanding compressor fouling. The present work scopes are devoted (i) to giving a reliable assessment, through experimental methods, of the mass deposited on the rotating and stationary airfoils of a compressor engine operating in a dust-laden flow and (ii) testing literature based deposition models, by employing numerical methods, for the prediction of the fouling rate on a real machine. The experimental investigation aims to reproduce the operative conditions of near-ground operations (in terms of ingested dose) and measure the mass deposited on the airfoils. The numerical approach, employing different sticking models available in the literature, is proposed as a benchmark for estimating the prediction capability in terms of deposited dust.

2. Materials and Methods

The present section is composed of two parts: the first one aims to describe the test facility and the experimental procedure of the fouling test and deposit collection, while in the second part, the numerical methods and the sticking models are explained in detail.

2.1. Experimental Investigation

The experimental investigation on particle deposition was carried out on the rotating test bench located in the Fluid Machinery Laboratory of the University of Ferrara, Italy. The test bench mounts the multistage compressor of the Allison 250 C18 engine [22]. A schematic view of the whole engine is reported in Figure 3a, while the picture of the compressor test unit is shown in Figure 3b. The axial part of the compressor unit, thanks to its small size, can be easily dismounted by removing the stator case and allowing direct access to the stator vanes and rotor blades. The pictures of the rotor wheel and stator vanes are reported in Figure 3c,d. A schematic layout of the test facility is reported in Figure 4. The same test bench was used for previous investigations about compressor fouling [14,23] and washing [24,25]. More details are reported there, and the most relevant features are reported here for the sake of completeness.

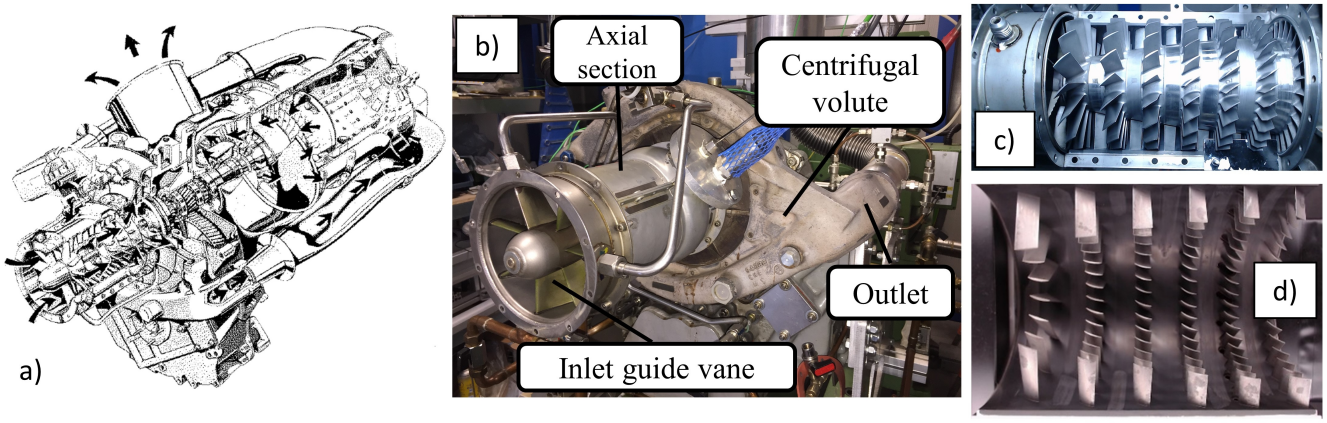

Figure 3. Allison 250 C18: (**a**) schematic view of the engine (taken from [22]); (**b**) side view of the compressor unit test bench; (**c**) rotor wheel; and (**d**) stator vanes.

The compressor unit has an inlet diameter of 0.104 m, and it is equipped with a fixed inlet guide vane (IGV). The compressor has six axial stages and one centrifugal stage. In correspondence with the 5th axial stage, a bleed valve is located, which is closed in the present application. The centrifugal stage has two semivolutes, each with a circular exit duct with a diameter of 0.056 m, and two flexible tubes link the outlet ducts to an exhaust outlet with a diameter of 0.100 m. An electric motor drives the compressor. The pressure ratio achieved at nominal operative conditions is 6.2, with a rotational speed of 51,600 rpm and a mass flow rate of 1.36 kg/s. The discharge section is composed of a plenum, a mass flow meter, and a throttle valve.

The test bench is equipped with a dust injection system, which provides a constant and controlled amount of contaminants toward the compressor's inlet. The system is driven by shop air provided by a screw compressor, which is equipped with a dryer and a set of filters to provide dry and clean air. The aerosol feeder, the SAG 410 Ultra-low Flow model, made by TOPAS GMBH, provides a continuous and precise dosage of the powder mass. An eductor is employed to disperse the dust, previously dosed by the feeder, into the compressor pipeline. Before entering the compressor unit, a 2 m length equilibrium tube was used to ensure the kinetic equilibrium between particles and air. This section ensures the proper mixing process to reach a uniform particle concentration at the compressor inlet. At the test bench inlet section, a compact filter EPA F9 class is placed to remove any possible contamination from the outside.

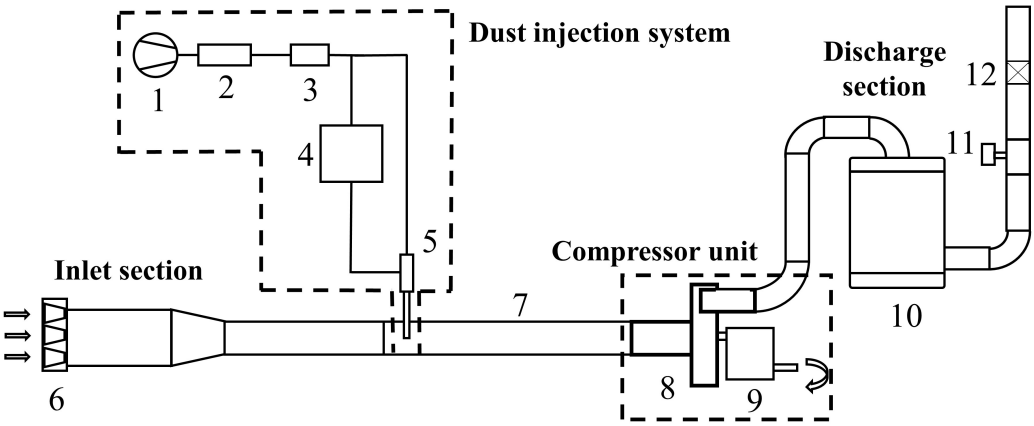

1 – Screw compressor	5 – Aerodynamic eductor	9 – Electric motor
2 – Drier	6 – Inlet filter	10 – Plenum
3 – Air filter	7 – Equilibrium length	11 – Mass flow meter
4 – Aerosol feeder	8 – Allison 250 C18 compressor	12 – Throttle valve

Figure 4. Schematic layout of the test rig.

2.1.1. Test Conditions

To reproduce the operative conditions encountered during ground and near-ground operations of rotorcraft engines in dusty environments, the concept of the dose of ingested contaminants (discussed in Section 1) was adopted. According to the operative range reported in Figure 2 for such operations, a representative dose value of 9.5 mg s/m^3 was selected. This value corresponds to the constant dose line reported in Figure 2.

The contaminant selected for this experimental test was the Arizona Road Dust (ARD) Nominal 0–3 µm (with a mean diameter of 1.1 µm and with 90% of the particles below 1.9 µm) provided by Powder Technology Inc. and obtained in agreement with ISO 12103-1:2016 [26]. The present contaminant is well-suited for compressor fouling tests due to its fine diameter distribution. More information about the ARD's physical and chemical properties, employed in the present campaign, can be found in [23].

The compressor unit was kept at 20,000 rpm, corresponding to a mass flow rate swallowed of 0.33 kg/s. This value of the corrected rotational speed corresponds to a sub-idle condition for the engine, which is a typical operative point in ground operations. The test facility is located in a closed room where the air was maintained at constant conditions of 22 °C ± 0.5 °C and 50% RH ± 3% RH during the test. The compressor was operated for 30 min with a constant dust mass flow rate ingested of 5.13 mg/s, leading to a concentration of 19 mg/m^3. Hence, the total mass ingested by the compressor was 9 g. After the particle ingestion operation, the case of the axial section of the compressor was disassembled, and the deposit collection process was carried out.

2.1.2. Deposit Collection Technique

The dust adhered on the compressor vanes and blades after the fouling process was measured employing an purposely designed device, the localized aspirator for particle observation (LAPO). The schematic view of the LAPO is depicted in Figure 5. This device is employed for particle sucking and collection from surfaces. It is driven by a vacuum pump (not shown in Figure 5). Thanks to its characteristics of compactness (100 mm total length) and lightness, the LAPO can be quickly oriented by the operator towards the compressor region to be analyzed. One of the LAPO's main components is the stainless steel needle, with an outer diameter of 1 mm, which ensures a direct particle sucking from the surface of interest. As shown in Figure 5, the needle, thanks to its thinness, can collect the powder in a very accurate manner from the surfaces. In Figure 5, the deposit collection operation from a leading edge is shown.

The LAPO is equipped with a filter that allows particle trapping, collection, and offline weighing. The filter type is a Grade 589/3 paper filter with a thickness of 0.15 mm, provided by Whatman plc. The filter remained locked and sealed during the sucking operation thanks to the coupling of the body's two parts through a screwed profile. At the end of the particle collection, the device was unscrewed, and the filter was removed and weighed. The weighing process was done employing the analytical balance Kern ABT 100-5NM model, with a resolution of 0.01 mg. The LAPO's particle collection capability was tested by sucking a dosed amount of ARD previously deposited on a test surface. An excellent capability to collect and trap the deposited particles was observed: the difference between the filter collected mass and the deposited mass was lower than 2%. Employing this collection technique, three zones of airfoils were analyzed: the leading edge (LE), the pressure side (PS), and the suction side (SS). The deposit collection operation was repeated for all the compressor airfoils of the stages (the IGV, the six stator vanes, and the six rotor blades). To improve the consistency of the present method, the deposit mass values, reported in the following section, result from the averaging process carried out by collecting the deposits on the surfaces belonging to the same row. This operation simplifies the weighing process and reduces the uncertainty of the entire deposit measurement.

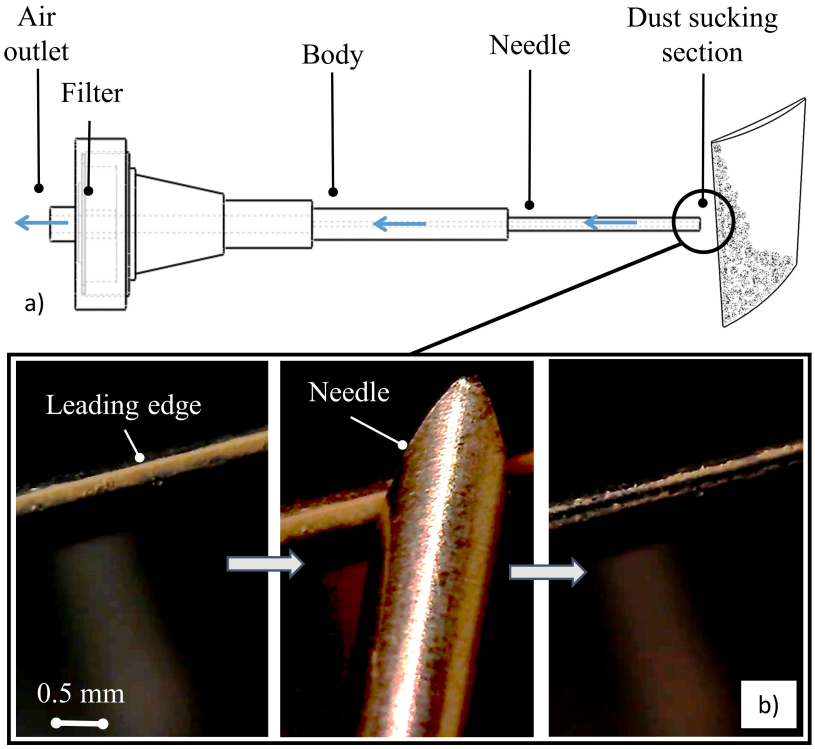

Figure 5. Particle collection device and operation: (**a**) schematic view of the localized aspirator for particle observation (LAPO), where the main zones of the device and the components are labeled and the air flow path is highlighted by the arrows; and (**b**) particle collection operation on the leading edge.

2.2. Numerical Approach and Sticking Models

The starting point of the numerical investigation is the result obtained by Aldi et al. [27]. The Allison 250 C18 axial compressor section's numerical simulations were carried out employing the commercial CFD code ANSYS CFX 13.0 [28], and all the details related to the CFD model were reported in [27]. For the scope of the present work, a multi-phase simulation was carried out. The solution approach for the particle trajectory calculation was based on a mathematical model with Eulerian conservation equations for the continuous phase and a Lagrangian frame to simulate a discrete second phase. After the simulation of the gas flow field, the trajectories of individual particles were tracked by integrating a

force balance equation on the particle. All the details related to the multi-phase numerical approach can be found in [29]. A total of 500,000 representative particles were injected at the compressor inlet section in the present work, employing the proper particle size distribution. The particle tracking allows predicting the coordinates, velocity, and angle of the particle impacts on surfaces of interest. Once the particles' impact properties are established, the implementation of a sticking model is essential for predicting whether the particle sticks to the surface or not. In the present work, two different models were implemented: Poppe et al.'s model [30] (including an addition related to the detachment effect), named in the present work as the silica carbide adhesion (SCA) model, and the Ohio State University (OSU) model [31]. The equations and the assumption based on these models are explained in detail in the following sections.

2.2.1. SCA Model

The experimental investigation carried out by Poppe et al. [30] and performed using micrometric silicon carbide particles impacting on a silica target provided an empirical relation for the calculation of the probability (sticking probability) of a particle adhering to a surface, based on its normal impact velocity value. The successful implementation of such a model to estimate the fouling rate on the NASA Rotor 37 can be found in [21]. The sticking probability (S_p) is calculated as follows:

$$S_p = \begin{cases} 0.99 - 0.09\, v_{1,n}, & \text{if } v_{1,n} \leq 4\ \text{m/s} \\ 2 \times 10^{-6}\, {v_{1,n}}^3 - 0.000378\, {v_{1,n}}^2 + 0.011800\, v_{1,n} + 0.587100, & \text{if } 4\ \text{m/s} < v_{1,n} < 90\ \text{m/s} \\ 0, & \text{if } v_{1,n} \geq 90\ \text{m/s} \end{cases} \quad (1)$$

where $v_{1,n}$ is the normal component of the particle impact velocity. As can be noted from Equation (1), the sticking probability values go from 0 to 1. According to the approach reported in [32], after the calculation of the sticking probability value, the result was compared to a chosen random number in the range [0,1] with a Gaussian distribution. If the random number is greater than the calculated value of the sticking probability, the particle does not stick, and vice versa. Through the application of this approach, the stochastic nature of the deposition process was taken into account.

The SCA model can be extended to include the contribution of the detachment effect. Following a similar approach reported in [33], the relation derived by Konstandopoulos [34] was implemented to account for a critical impact angle (α_{crit}) based on an energy balance between the tangential kinetic energy of the particle and the minimum energy required to break its contact area with the surface. The expression for the critical angle is:

$$tan(\alpha_{crit}) = \left(\frac{v_{1,t}}{v_{1,n}}\right)_{crit} = 0.034021 \frac{f}{\beta^{3/2}} \sqrt{2\frac{2-\nu}{1-\nu}} \quad (2)$$

where $v_{1,t}$ is the tangential component of the particle impact velocity, f is the friction coefficient between the particle and the surface, ν is the Poisson's ratio of the particle-surface pair, and β is a numerical constant (a suggested value is 0.63). The addition of the critical angle formulation to the sticking model acts as a filter for the particle deposition: if the impact angle exceeds the critical value, the particle is not supposed to stick on the wall (leading to a null value of the sticking probability). Depending on the presence or not of a third substance at the interface between particle and substrate, the values of f and ν shall be modified. In dry conditions (absence of a third substance at the particle-substrate interface), the values of 0.5 and 0.3 are assigned to f and ν, respectively. If a liquid layer is located between the particle and substrate, the value of ν becomes 0.4, while the friction coefficient is calculated according to the relation:

$$f = \frac{64}{Re_p} \quad (3)$$

where Re_p is the particle Reynolds number, defined as:

$$Re_p = \frac{\rho_p v_{1,n} d_p}{\mu} \tag{4}$$

where ρ_p is the particle material density, d_p is the particle diameter, and μ is the liquid viscosity.

2.2.2. OSU Model

Bons et al. [31] proposed a theoretical model for the prediction of rebound and deposition in gas turbine engines. The model accounts for the particle elastic-plastic deformation, adhesion, and shear removal. Thanks to its explicit and parametric formulation and the particle material properties' dependence, the model is general and well-suited for the implementation in CFD codes. Unlike the SCA model, which foresees the sticking probability's computation, the OSU model is based on the calculation of the normal component of the coefficient of restitution (COR_n). COR_n is defined as the ratio between the kinetic energy of the rebounding particle ($E_{kin,v_{2,n}}$) and the kinetic energy of the impacting particle ($E_{kin,v_{1,n}}$). In the OSU model, the particle is modeled as a cylinder, which is deformed when it impacts the surface. The particle impact can be defined as elastic, if the deformation (w) remains below its critical value (w_{crit}), or plastic, if the deformation exceeds it. The critical value of the deformation depends only on the particle material properties, and it is defined as:

$$w_{crit} = \frac{\sigma_{y,p}\, l}{E_{Y,c}} \tag{5}$$

where $\sigma_{y,p}$ is the particle yield stress, $E_{Y,c}$ is the composite Young modulus, and l is equal to $\frac{2}{3}\, d_p$. The composite Young modulus is calculated according to the following relation:

$$E_{Y,c} = \left(\frac{1 - {\nu_p}^2}{E_{Y,p}} + \frac{1 - {\nu_w}^2}{E_{Y,w}} \right)^{-1} \tag{6}$$

where ν_p and $E_{Y,p}$ are the Poisson's ratio and Young's modulus of the particle and ν_w and $E_{Y,w}$ are the Poisson's ratio and Young's modulus of the wall material.

The normal component of the rebounding particle kinetic energy ($E_{kin,v_{2,n}}$) can be computed as:

$$E_{kin,v_{2,n}} = \begin{cases} E_{kin,v_{1,n}} - W_a, & \text{if } w \leq w_{crit} \\ E_{crit} + M_{drag} - W_a, & \text{if } w > w_{crit} \end{cases} \tag{7}$$

where $E_{kin,v_{1,n}}$ is the normal component of the impacting particle kinetic energy, W_a is the work of adhesion, E_{crit} is the maximum elastic energy storage, and M_{drag} is the drag moment of the shear stress acting on the particles. The formulation of the maximum elastic energy storage is:

$$E_{crit} = \frac{V\, {\sigma_{y,p}}^2}{2\, E_{Y,c}} \tag{8}$$

where V is the volume of the particle. The expression of the work of adhesion is the following:

$$W_a = \pi\, \gamma\, {a_{cont}}^2 \tag{9}$$

where γ is the surface free energy and a_{cont} is the contact radius, which can be derived from the expression of the contact area through the relation $a_{cont} = \sqrt{A_{cont}/\pi}$. The contact area is derived employing a semi-empirical relation:

$$A_{cont} = \left[a + b \left(\frac{w_{max}}{w_{crit}} \right)^c \right] A_{crit} \tag{10}$$

where w_{max} is the maximum plastic deformation of the particle and A_{crit} is the particle contact area at the end of the elastic deformation ($V/(l - w_{crit})$). The constants a, b, and c have the values of 1/10, 1/7, and 1/2, respectively. The maximum plastic deformation of the particle can be calculated employing the following relation:

$$w_{max} = l - exp\left(\ln(l - w_{crit}) - \frac{E_{kin,v_{1,n}} - E_{crit}}{\sigma_{y,p}\, V}\right) \tag{11}$$

Finally , the drag moment in Equation (7) is computed as:

$$M_{drag} = \frac{{\rho_a}^3\, {u_\tau}^4\, d_p\, l^4}{8\, {\mu_a}^2} + \frac{3{\rho_a}^{5/3}\, {u_\tau}^{8/3}\, d_p^{1/3}\, l^{10/3}}{2{\mu_a}^{2/3}} \tag{12}$$

where ρ_a is the air density, u_τ is the wall shear velocity, and μ_a is the air viscosity. The knowledge of the normal component of the kinetic energy values at the impact ($E_{kin,v_{1,n}}$) and rebound ($E_{kin,v_{2,n}}$) stages allows calculating the normal component of the coefficient of restitution (COR_n) for the particle, according to the relation:

$$COR_n = \sqrt{\frac{E_{kin,v_{2,n}}}{E_{kin,v_{1,n}}}} \tag{13}$$

If the COR_n calculation returns zero, the particle sticks to the surface, and vice versa, a rebound occurs.

The OSU model is based on the particle and wall material constants. The use of widespread engineering materials (such as steel, aluminum alloy, titanium alloy, etc.) in the machining of the compressor components makes the mechanical properties of the wall easy to obtain. In contrast, the values of the particle material properties are characterized by a certain degree of uncertainty, which may affect the reliability of the sticking model results. The mechanical properties of the particles, employed in the present study, were taken from [31], while the wall material properties refer to those of a stainless steel. The numerical values of the material properties are reported in Table 1.

Table 1. Mechanical properties of the Arizona Road Dust particle and wall materials.

ρ_p	$\sigma_{y,p}$	$E_{Y,p}$	$E_{Y,w}$	ν_p	ν_w
2700 kg/m^3	110–130 MPa	104 GPa	196 GPa	0.18	0.29

Bons et al. [31] suggested a fixed value of the surface free energy (γ) equal to 0.8 N/m. Such a parameter is difficult to evaluate, and in the present study, three values of γ were considered: 0.8 N/m, which is the value suggested in [31]; 0.4 N/m, which is a value obtained according to the low of mixtures for ARD in [35]; and 0.1 N/m, which is an arbitrary value, chosen to extend the sensitivity analysis.

In Figure 6, the surface plot of COR_n as a function of the particle diameter and normal impact velocity is proposed. The charts refer to three values of γ equal to 0.1 N/m (Figure 6a), 0.4 N/m (Figure 6b), and 0.8 N/m (Figure 6c). COR_n has been reported for a fixed value of u_τ equal to 15 m/s, which is an intermediate value between those reported in [31]. The increase of the surface free energy value leads to an overall decrease of COR_n towards null values for the finest particles. This behavior is strictly related to the high value of the work of adhesion obtained for the finest diameter range, which overrides the kinetic energy available for the rebound in Equation (7).

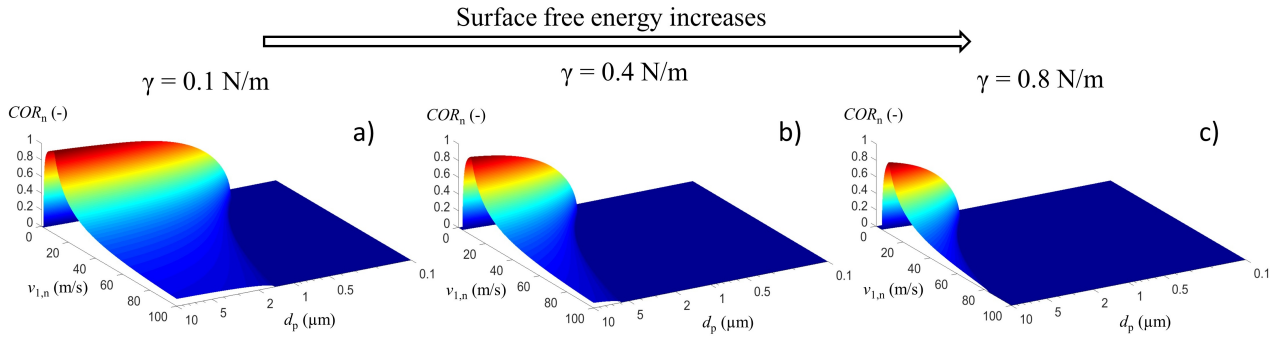

Figure 6. Surface plot of COR_n calculated according to the Ohio State University (OSU) model [31] for a fixed value of the wall shear velocity, equal to 15 m/s. The charts refer to: (**a**) γ = 0.1; (**b**) γ = 0.4; and (**c**) γ = 0.8.

3. Results and Discussion

In the present section, the experimental measurement and the numerical results are shown and compared.

3.1. Dust Collection Measurements

According to the procedure reported in Section 2.1.2, the mass collected on each filter is divided for the respective number of airfoils of each row. For completeness, the number of airfoils of each stage's row reported in Table 2.

In Figure 7, the particle collection process results are depicted, and the error band is related to the total mass collected on the airfoils. The error band scale follows from the combination of the uncertainties associated with the weighing process and the filter collection capability, reported in Section 2.1.2.

The trend of the mass deposited on the single airfoil (over the stages) is in line with the results reported in [36–38]. The fouling rate is higher for the airfoils of the first stages (particularly on the IGV) and decreases over the six axial stages. These observations agree with the literature findings: a higher fouling rate is often detected in correspondence with the machine's first stage airfoils. In contrast, the airfoils of the aft stages are less affected by the particle deposition issue. The observed trend may be explained by accounting for the different thermodynamic and kinetic effects, which coexist and influence the interaction between the airfoil surface and the particle.

Regarding the thermodynamic effect, the presence of moisture may affect the magnitude of the dust adhered to the first stages of the compressor. Due to the flow acceleration achieved in the inlet bell-mouth, a sudden drop in the air pressure and temperature occurs. Hence, the combination of these effects can bring the moisture present into the air to condense in saturated conditions [39], increasing the powder's stickiness due to the "glue-action" of the condensed droplets. Across the stages, the increase of the flow temperature moves the air away from the saturated condition, leading to a reduction of this effect. The increased air velocity over the stages may promote the particle bounce instead of adhesion and may increase the removal action on the deposit due to the shear velocity [40].

In order to give a more general perspective of the deposition process, an overview of the mass deposited on the compressor flow path (for the single airfoil, row, and stage) divided by the total mass injected into the compressor is reported in Table 2 employing non-dimensional quantities. The ratio between the mass deposited on the single airfoil and the total mass ingested ($m_{d,airfoil}/m_{ing}$) shows similar results to those reported in Figure 7: the amount of the mass deposited for the single airfoil reduces over the stages. By looking at the ratio between the mass deposited on the row and the total mass ingested ($m_{d,row}/m_{ing}$), it can be assessed that, on average, the stator vanes are more prone to fouling, with respect to the rotor blades. This fact can be explained by accounting for the different dynamic effects on the particles, which arise in stationary and rotating channels. The mass ratio related to the stage ($m_{d,stage}/m_{ing}$) has an overall decrease over the compressor flow

path, except for the fifth stage. In that position, the stator vanes collect a higher amount of dust, probably due to the bleed valve's presence, which generates a disturbance for the flow-field. The general report allows assessing that almost 1.6% of the total mass ingested is collected by the compressor airfoils.

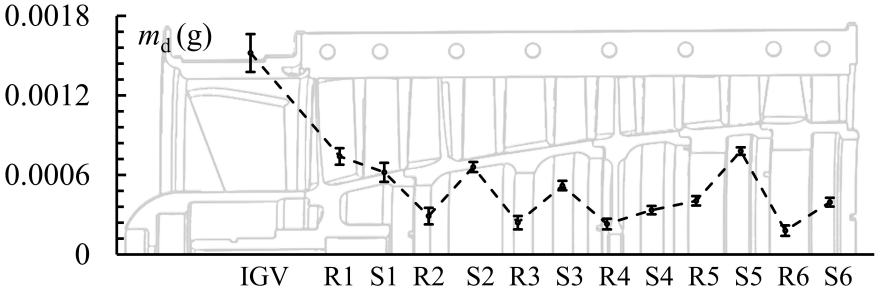

Figure 7. Mass deposited on a single airfoil for each row of the compressor unit.

Table 2. Airfoil number and overview of the mass deposited on the single airfoil, row, and stage.

Position	IGV	Stage 1		Stage 2		Stage 3		Stage 4		Stage 5		Stage 6	
		R1	S1	R2	S2	R3	S3	R4	S4	R5	S5	R6	S5
Airfoil number	7	16	14	16	26	20	28	25	32	28	36	25	30
$m_{d,airfoil}/m_{ing}$ (%)	0.016	0.008	0.007	0.003	0.007	0.003	0.006	0.002	0.004	0.004	0.008	0.002	0.004
$m_{d,row}/m_{ing}$ (%)	0.120	0.130	0.090	0.050	0.190	0.050	0.160	0.060	0.120	0.120	0.300	0.050	0.130
$m_{d,stage}/m_{ing}$ (%)	0.120	0.220		0.240		0.210		0.180		0.430		0.180	

In Figure 8, the percentage of the mass deposited on the leading edge, pressure side, and suction side, concerning the total mass collected from each vane and blade, is shown. Moving from the IGV to the aft stages, the deposit collection increases progressively on the PSs and decreases on the SSs. This effect is higher on the stationary airfoils with respect to the rotating ones. Moreover, a significant increase in the deposits on the leading edge is observed. These effects are strictly related to the fluid dynamic flow field inside the compressor: a well-oriented flow towards the latter stages of the compressor may lead to reduced vane separation phenomena. Similar findings were also observed in the investigation of Tarabrin et al. [37] on the 16 stage axial compressor of the Nuovo Pignone MS5322R.

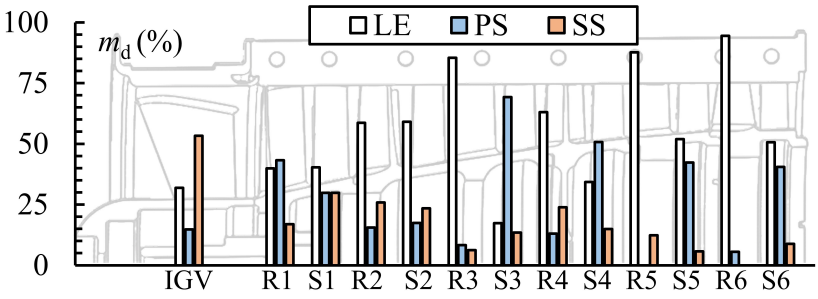

Figure 8. Percentage of the mass deposited on the leading edge (LE), pressure side (PS), and suction side (SS) with respect to the total mass deposited on the single airfoil.

3.2. Numerical Results and Sticking Model Application

The multi-phase numerical simulation carried out on the axial part of the Allison 250 C18 compressor unit allows obtaining the information related to the impact behavior of the solid particles. Starting from these quantities, the sticking capability on the compressor vanes and blades can be assessed by employing the models reported in Section 2.2. Figure 9 reports the impact location on the airfoils, highlighted according to their normal impact velocity (Figure 9a) and impact angle (Figure 9b). The airfoils' PSs are almost entirely

affected by particle impacts, while the impacts on the SSs are located mostly near the stator case.

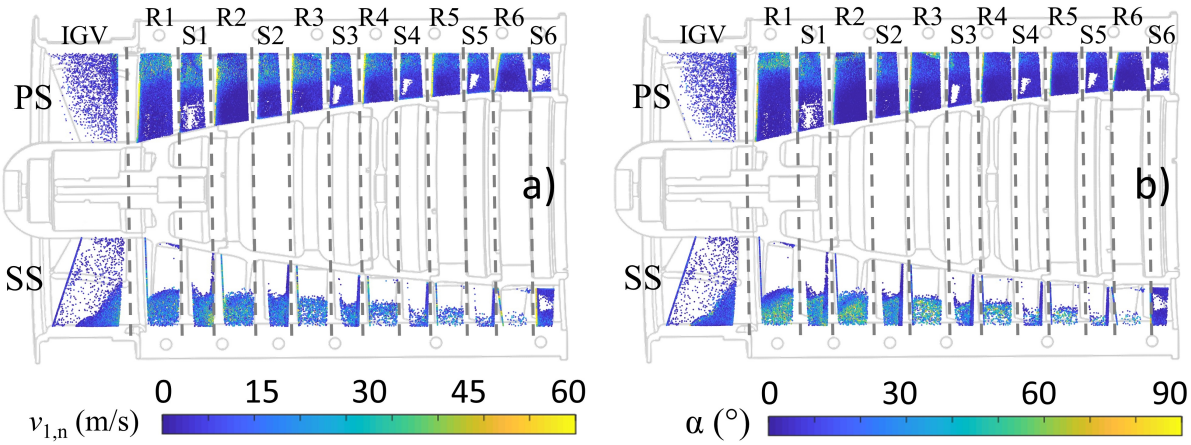

Figure 9. Particle impact behavior over the compressor stages: (**a**) normal impact velocity; and (**b**) impact angle.

The impact velocity and angle results are strongly influenced by the fluid dynamic conditions in which the compressor has been operated. As reported in Section 2.1.1, during the test, the compressor was kept at a sub-idle rotational regime, leading to an off-design operation of the machine. This condition causes the presence of flow separation zones in correspondence with the compressor airfoils. This finding is highlighted in Figure 10a, where the airfoils' surface streamlines are depicted. The flow separation zones are located mainly on the SSs of the airfoils, near the compressor case, and to a minor extent on the PSs of the first stage airfoil. The spread of the separation zones seems to reduce towards the aft stages of the compressor. Comparing Figures 9 and 10a, the presence of the SS separation seems to be the main aspect responsible for the particle impact on these zones. The finest particles are more prone to be subjected to turbulent diffusion due to their lower inertia, leading to a higher propensity to be trapped by turbulent eddies. Consequently, the reduction of the separation zones towards the aft stages leads to fewer particle impacts on the SSs of the airfoils. The experimental measurements reported in Figure 8 agree with this finding.

An example of the turbulent eddies effect on the particle motion can be observed on the SS of the IGV: an extended separation zone is located near the vane's trailing edge, highlighted in Figure 10a. A picture of the airfoil after the particle ingestion operation is reported in Figure 10b, proving a high particle collection capability in correspondence with this zone.

As an intermediate step towards the deposited mass assessment via the numerical approach, the calculation of the sticking probability, S_p (for the SCA model), and the coefficient of restitution, COR_n (for the OSU model), is needed. The sticking probability results obtained using the SCA model are reported in Figure 11, showing how the deposition process changes according to the model adopted.

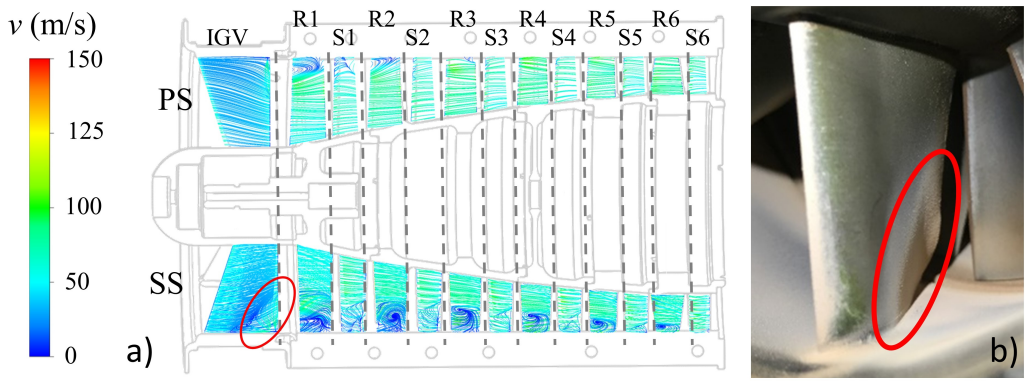

Figure 10. Surface streamlines on the airfoils over the compressor flow-path (**a**) and the SS of the compressor IGV with the separation zone highlighted (**b**).

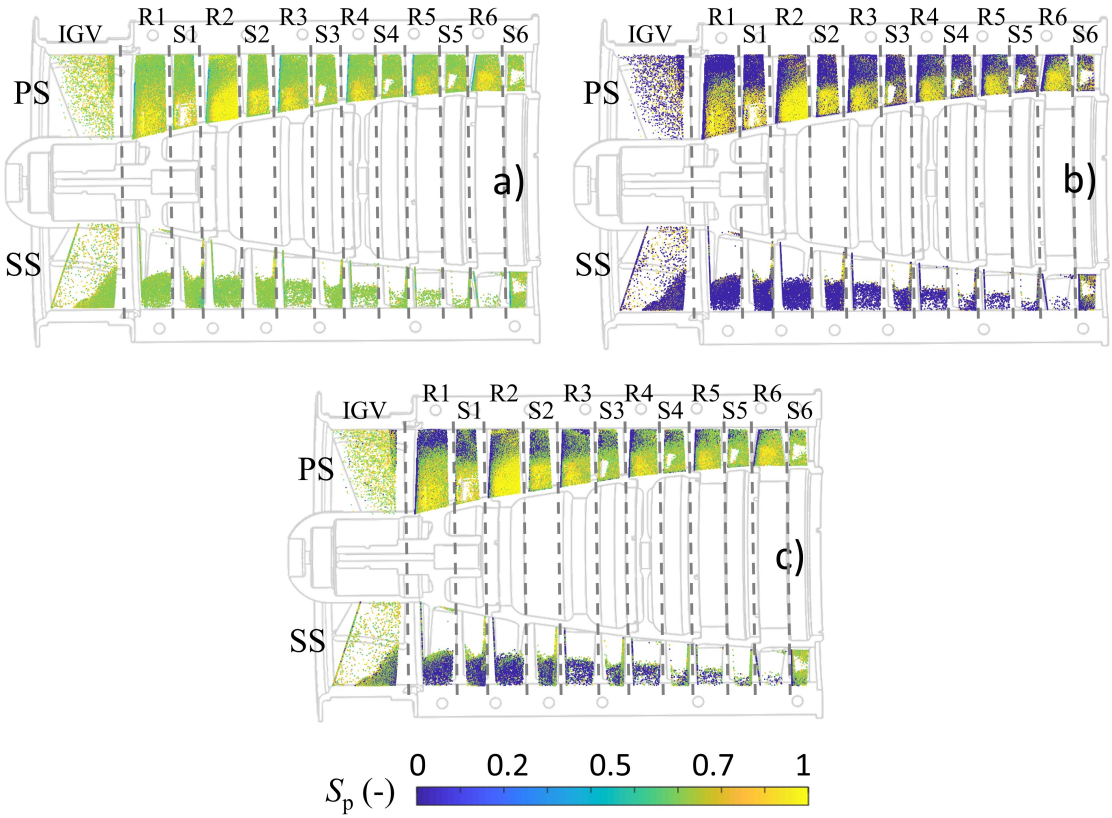

Figure 11. Sticking probability calculated over the compressor stages: (**a**) silica carbide adhesion (SCA) model; (**b**) SCA model with critical impact angle in dry conditions; and (**c**) SCA model with critical impact angle in wet conditions

The SCA model application leads to sticking probability values greater than 0.6 over the compressor flow path (Figure 11a). This is due to an averaged low value of the normal impact velocity (Figure 9a), which increases the sticking probability, according to Equation (1). The component related to the critical angle has the result of decreasing the overall sticking probability across the stages, as shown in Figure 11b,c. The critical angle formulation in dry conditions leads to a significant decrease of S_p in correspondence with the SSs and a portion of the PSs near the case (Figure 11b). The addition of the third substance among the particle and the surface leads to intermediate results (Figure 11c).

The results of the OSU model implementation are reported in Figure 12 for a value of γ of 0.1 N/m (Figure 12a) and 0.4 N/m (Figure 12b) respectively, and for a particle yield stress value of 130 MPa.

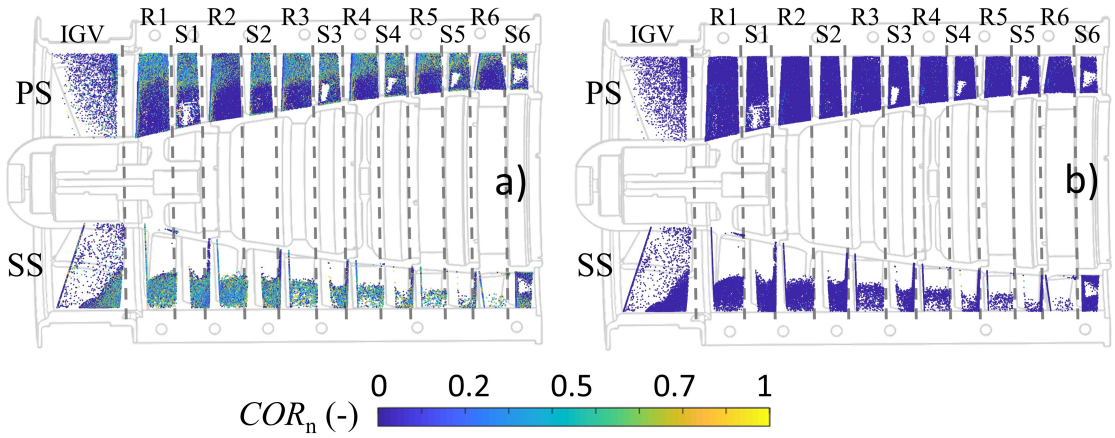

Figure 12. COR_n calculated over the compressor stages for (a) γ = 0.1 N/m and (b) γ = 0.4 N/m.

COR_n has a significant dependence on the value of the surface free energy, as shown also in Figure 6. Values of γ of 0.4 N/m and 0.8 N/m return null values of COR_n for a wide range of particle impacts. This finding is justified by the small size range of the particles employed in the present analysis (below 3 µm), which is located almost entirely in the zone of null COR_n in Figure 6b,c. For this reason, the use of such values of surface free energy leads to a condition of "perfect adhesion", meaning that each impacting particle (belonging to the diameter distribution tested in the present work) sticks to the surface. The use of a surface free energy value of 0.1 N/m leads to results comparable to the SCA model, in terms of deposited patterns.

3.3. Comparison between Experimental and Numerical Results

Starting from the previous section results, the mass adhered to the compressor airfoils was calculated. Since a stationary simulation was carried out, the deposited mass was calculated, on the first instance for a unit of time, obtaining the particle mass flow rate on the surfaces, and then extended to the operative time in which the compressor unit was tested. This procedure was carried out by scaling the representative particle flow rate, injected in the CFD simulation, to the actual particle mass flow rate employed during the experimental test, according to [28]. The assumption made at this point is that the adhesion process is linear and does not depend on the pre-existing particle layer.

In Figures 13 and 14, the comparison between the numerical results and the experimental values are reported for the SCA model and the OSU model, respectively. As can be noted, the numerical simulations return an overestimation of the amount of deposits for all the tested models of almost one order of magnitude. This spread may be related to the complexity of the tracking of fine particles, whose motion is affected by the turbulent dispersion and diffusion mechanisms that govern it. Moreover, the difficulty related to the choice of reliable constants for the sticking/rebound models is another issue to deal with, when the deposition process is simulated. The combination of the error sources associated with these aspects may represent the main cause of the spread between experimental observation and numerical results. Although, due to the intrinsically complex nature of particle deposition phenomena, the magnitude of the spread found with the present approach could be considered acceptable for industrial scopes.

The SCA model (Figure 13) gives lower values of deposits with respect to the OSU model (Figure 14), and the difference increases towards the aft stages of the compressor. This is mainly due to the increase of the particle impact velocity in the compressor's last stages, leading to the reduction of the sticking probability. In both dry and wet conditions, the addition of the critical angle formulation results in a downward shift of the deposited mass values. In particular, the dry condition gives a significant reduction of the deposited mass, leading to good results, especially on the compressor IGV, whose deposited mass value is close to the experimental finding.

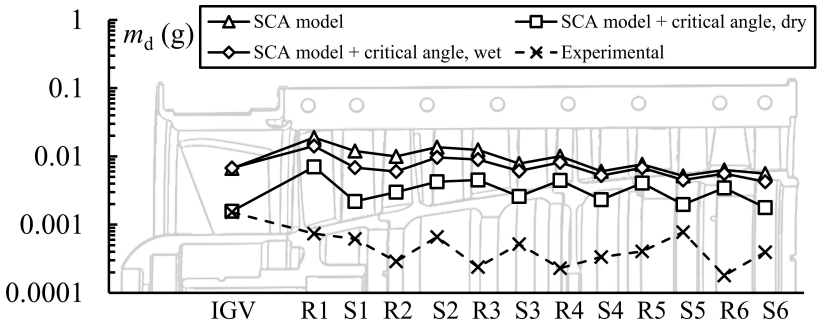

Figure 13. Comparison between the SCA model results and experimental values of the deposited mass on the compressor airfoils.

The OSU model predicts a higher amount of deposits. The calculation of COR_n was carried out with two values of particle yield stress (110 MPa and 130 MPa) and three values of surface free energy (0.1 N/m, 0.4 N/m, and 0.8 N/m). The setup with surface free energy values of 0.4 N/m and 0.8 N/m increases the value of the work of adhesion, overwhelming the maximum storage energy term (E_{crit}) in Equation (7). Such a condition returns null values of COR_n, leading to the adhesion of most of the impacting particles. For such values of γ, the influence of the variation of the particle yield stress value seems to be ineffective. The use of a surface free energy value of 0.1 N/m leads to a significant decrease of the deposited mass, and in such a condition, the influence of the particle yield stress is evident. The OSU model is well suited when airfoils are covered by a uniform oil or grease layer, leading to the increase of the adhesion forces between particles and the surface, as shown in Casari et al. [41].

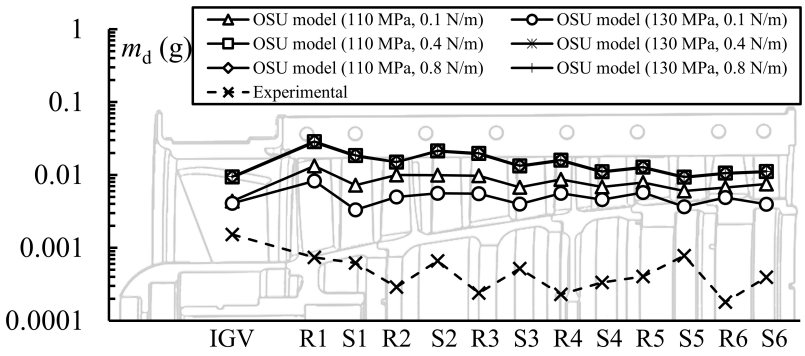

Figure 14. Comparison between the OSU model results and experimental values of the deposited mass on the compressor airfoils.

4. Conclusions

In this work, a comprehensive study of micrometric particle adhesion on the airfoils of a rotorcraft engine compressor is carried out. The research aims to assess the fouling rate of the compressor rotor blades and stator vanes employing experimental and numerical methods.

The experimental test is carried out on a rotating test facility, which mounts the Allison 250 C18 engine compressor, by injecting micrometric test powder to simulate a ground-idle operation. At the end of the test, the collection of the deposits from the airfoils is provided. The particle collection and measurement operations show that the deposited mass on the airfoils decreases towards the compressor's last stages, where the high velocity promotes rebound instead of deposition. By comparing the total mass collected from the airfoils to the mass swallowed by the compressor, it can be assessed that almost 1.6% of the total ingested mass sticks to the vanes and blades.

Two sticking models available in the literature are implemented, employing numerical methods, with the aim to test their capability to predict the fouling rate on the airfoil surfaces. From the comparison between the numerical flow field, numerical impact zones,

and the observed patterns, it seems that the presence of separation zones is responsible for the increase of the particle adhesion in a portion of the airfoils. The results of the sticking model implementation lead to the systematic overestimation of the mass deposited on the compressor airfoils. Regardless, the numerical results seem to be in line and give a good agreement in terms of relative results.

The spread between the experimental measurements and the numerical findings may be related to the complexity of fine particle tracking and the selection of reliable numerical constants for the sticking/rebound models. Even if the spread between numerical and experimental findings may be significant, the results could still be acceptable for industrial purposes in order to assess the fouling rate on a real machine.

Further research should be addressed to the investigation of the effects that promote detachment and rebound of particles and their reliable implementation in the CFD environment.

Author Contributions: Conceptualization, A.V., A.S.; methodology, A.V., A.S.; investigation, A.V., A.S.; data curation, A.V.; writing—original draft preparation, A.V.; writing—review and editing, A.S., N.C., M.P.; supervision, M.P. All authors have read and agreed to the published version of the manuscript.

Funding: This research received no external funding.

Conflicts of Interest: The authors declare no conflict of interest.

References

1. Wadcock, A.J.; Ewing, L.A.; Solis, E.; Potsdam, M.; Rajagopalan, G. *Rotorcraft Downwash Flow Field Study to Understand the Aerodynamics of Helicopter Brownout*; Technical Report; US Army Aviation and Missile Command, Army/NASA Rotorcraft Division, Army Aeroflightdynamics Directorate (AMRDEC): Moffett Field, CA, USA, 2008.
2. Mapes, P.; Kent, R.; Wood, R. *DoD Helicopter Mishaps FY85-05: Findings and Recommendations*; Department of Defense: Washington, DC, USA, 2008.
3. Dunn, M.G.; Padova, C.; Moller, J.; Adams, R. Performance deterioration of a turbofan and a turbojet engine upon exposure to a dust environment. *J. Eng. Gas Turbines Power* **1987**, *109*, 336–343. [CrossRef]
4. Edwards, V.R.; Rouse, P.L. US army rotorcraft turboshaft engines. In *AGARD Conference Proceedings*; AGARD: Neuilly-sur-Seine, France, 1994; pp. 31–310.
5. Rapp, G.; Rosenthal, S. Problems and solutions for sand environment operation of helicopter gas turbines. In Proceedings of the ASME 1968 Gas Turbine Conference and Products Show, Washington, DC, USA, 17–21 March 1968.
6. Suman, A.; Morini, M.; Aldi, N.; Casari, N.; Pinelli, M.; Spina, P.R. A Compressor Fouling Review Based on an Historical Survey of ASME Turbo Expo Papers. *J. Turbomach.* **2017**, *139*, 041005. [CrossRef]
7. Bammert, K.; Woelk, G. The influence of the blading surface roughness on the aerodynamic behavior and characteristic of an axial compressor. *J. Eng. Gas Turbines Power* **1980**, *102*, 283–287. [CrossRef]
8. Cowherd, C., Jr. *Sandblaster 2 Support of See-Through Technologies for Particulate Brownout*; Technical Report; Midwest Research Institute: Kansas City, MO, USA, 2007.
9. S76—Performance and Operations Handbook. In *The Australian Air Transport Pilot License (Helicopter)*; Civil Aviation Safety Authority, Australian Government: Woden, Australia, 2013.
10. Clarkson, R.J.; Majewicz, E.J.; Mack, P. A re-evaluation of the 2010 quantitative understanding of the effects volcanic ash has on gas turbine engines. *Proc. Inst. Mech. Eng. Part J. Aerosp. Eng.* **2016**, *230*, 2274–2291. [CrossRef]
11. Shao, Y.; Yang, Y.; Wang, J.; Song, Z.; Leslie, L.M.; Dong, C.; Zhang, Z.; Lin, Z.; Kanai, Y.; Yabuki, S.; et al. Northeast Asian dust storms: Real-time numerical prediction and validation. *J. Geophys. Res. Atmos.* **2003**, *108*. [CrossRef]
12. Bojdo, N.; Filippone, A. A Simple Model to Assess the Role of Dust Composition and Size on Deposition in Rotorcraft Engines. *Aerospace* **2019**, *6*, 44. [CrossRef]
13. Bojdo, N.; Filippone, A.; Parkes, B.; Clarkson, R. Aircraft engine dust ingestion following sand storms. *Aerosp. Sci. Technol.* **2020**, *106*, 106072. [CrossRef]
14. Vulpio, A.; Suman, A.; Casari, N.; Pinelli, M.; Kurz, R.; Brun, K. Analysis of time-wise compressor fouling phenomenon on a multistage test compressor: Performance losses and particle adhesion. *J. Eng. Gas Turbines Power* **2021**, doi:10.1115/1.4049505. [CrossRef]
15. Asplund, P. Gas turbine cleaning upgrade (compressor wash). *Turbo Expo Power Land Sea Air. Am. Soc. Mech. Eng.* **1997**, *78675*, V001T09A003.
16. Friso, R.; Casari, N.; Suman, A.; Pinelli, M.; Montomoli, F. A Design for Fouling Oriented Optimization of an HPT Nozzle. *Turbo Expo Power Land Sea Air. Am. Soc. Mech. Eng.* **2019**, *58585*, V02DT47A014.

17. Döring, F.; Staudacher, S.; Koch, C.; Weißschuh, M. Modeling Particle Deposition Effects in Aircraft Engine Compressors. *J. Turbomach.* **2017**, *139*, 051003. [CrossRef]
18. Brun, K.; Grimley, T.A.; Foiles, W.C.; Kurz, R. Experimental Evaluation of the Effectiveness of Online Water-Washing in Gas Turbine Compressors. *J. Eng. Gas Turbines Power* **2015**, *137*, 042605. [CrossRef]
19. Kurz, R.; Musgrove, G.; Brun, K. Experimental Evaluation of Compressor Blade Fouling. *J. Eng. Gas Turbines Power* **2017**, *139*, 032601. [CrossRef]
20. Suman, A.; Kurz, R.; Aldi, N.; Morini, M.; Brun, K.; Pinelli, M.; Ruggero Spina, P. Quantitative computational fluid dynamics analyses of particle deposition on a transonic axial compressor blade—Part I: Particle zones impact. *J. Turbomach.* **2015**, *137*, 021009. [CrossRef]
21. Suman, A.; Morini, M.; Kurz, R.; Aldi, N.; Brun, K.; Pinelli, M.; Ruggero Spina, P. Quantitative Computational Fluid Dynamic Analyses of Particle Deposition on a Transonic Axial Compressor Blade—Part II: Impact Kinematics and Particle Sticking Analysis. *J. Turbomach.* **2015**, *137*, 021010. [CrossRef]
22. Allison Gas Turbine. *Operation and Maintenance Manual. Turboshaft Models 250-C18, A, B & C*; Detroit Diesel Allison, Division of General Motors Corporation: Indianapolis, IN, USA, 1975.
23. Suman, A.; Vulpio, A.; Casari, N.; Pinelli, M.; Kurz, R.; Brun, K. Deposition pattern analysis on a fouled multistage test compressor. *J. Eng. Gas Turbines Power* **2021**. [CrossRef]
24. Casari, N.; Pinelli, M.; Spina, P.R.; Suman, A.; Vulpio, A. Performance degradation due to fouling and recovery after washing in a multistage test compressor. *ASME J. Eng. Gas Turbines Power* **2021**, *143*, 031020 [CrossRef]
25. Casari, N.; Pinelli, M.; Suman, A.; Vulpio, A.; Appleby, C.; Kyte, S. Assessment of the washing effectiveness of on-purpose designed eco-friendly cleaner against soot deposits. *J. Glob. Power Propuls. Soc.* **2020**, *4*, 253–263. [CrossRef]
26. ISO. *Road Vehicles-Test Dust for Filter Evaluation-Part 1: Arizona Test Dust*; BSI-British Standards Institution: London, UK, 1997; pp. 1–6.
27. Aldi, N.; Morini, M.; Pinelli, M.; Spina, P.R.; Suman, A. Cross validation of multistage compressor map generation by means of computational fluid dynamics and stage-stacking techniques. In Proceedings of the ASME Turbo Expo 2014: Turbine Technical Conference and Exposition, Düsseldorf, Germany, 16–20 June 2014; p. V03BT25A009.
28. ANSYS. *Release 13.0-User Manual*; AQWA: Canonsburg, PA, USA, 2010.
29. Aldi, N.; Casari, N.; Pinelli, M.; Suman, A.; Vulpio, A.; Saccenti, P.; Beretta, R.; Fortini, A.; Merlin, M. Erosion behavior on a large-sized centrifugal fan. In Proceedings of the 13th European Turbomachinery Conference on Turbomachinery Fluid Dynamics and Thermodynamics, ETC 2019, Lausanne, Switzerland, 8–12 April 2019; pp. 1–8.
30. Poppe, T.; Blum, J.; Henning, T. Analogous experiments on the stickiness of micron-sized preplanetary dust. *Astrophys. J.* **2000**, *533*, 454. [CrossRef]
31. Bons, J.; Prenter, R.; Whitaker, S. A simple physics based model for particle rebound and deposition in turbomachinery. *J. Turbomach.* **2017**, *139*, V05BT11A007. [CrossRef]
32. Casari, N.; Pinelli, M.; Suman, A.; Mare, L.D.; Montomoli, F. An energy based fouling model for gas turbines: EBFOG. *J. Turbomach.* **2017**, *139*, 021002. [CrossRef]
33. Aldi, N.; Casari, N.; Dainese, D.; Morini, M.; Pinelli, M.; Spina, P.R.; Suman, A. Fouling on a multistage axial compressor in the presence of a third substance at the particle/surface interface. *Turbo Expo Power Land Sea Air. Am. Soc. Mech. Eng.* **2018**, *51029*, V02DT47A014.
34. Konstandopoulos, A.G. Particle sticking/rebound criteria at oblique impact. *J. Aerosol Sci.* **2006**, *37*, 292–305. [CrossRef]
35. Suman, A.; Casari, N.; Fabbri, E.; di Mare, L.; Montomoli, F.; Pinelli, M. Generalization of particle impact behavior in gas turbine via non-dimensional grouping. *Prog. Energy Combust. Sci.* **2019**, *74*, 103–151. [CrossRef]
36. Ashbrook, R.L. *A Survey of Salt Deposits in Compressors of Flight Gas Turbine Engines*; National Aeronautics and Space Administration: Washington, DC, USA, 1969; Volume 4999.
37. Tarabrin, A.; Schurovsky, V.; Bodrov, A.; Stalder, J.P. Influence of axial compressor fouling on gas turbine unit perfomance based on different schemes and with different initial parameters. In Proceedings of the ASME 1998 International Gas Turbine and Aeroengine Congress and Exhibition, Stockholm, Sweden, 2–5 June 1998; p. V004T11A006.
38. Syverud, E.; Brekke, O.; Bakken, L.E. Axial compressor deterioration caused by saltwater ingestion. *J. Turbomach.* **2007**, *129*, 119–126. [CrossRef]
39. Stalder, J.P. Gas Turbine Compressor Washing State of the Art—Field Experiences. In Proceedings of the ASME 1998 International Gas Turbine and Aeroengine Congress and Exhibition, Stockholm, Sweden, 2–5 June 1998; p. V004T11A010.
40. Suman, A.; Vulpio, A.; Fortini, A.; Fabbri, E.; Casari, N.; Merlin, M.; Pinelli, M. Experimental analysis of micro-sized particles time-wise adhesion: The influence of impact velocity and surface roughness. *Int. J. Heat Mass Transf.* **2021**, *165*, 120632. [CrossRef]
41. Casari, N.; Altmeppen, J.; Koch, C.; Pinelli, M.; Staudacher, S.; Suman, A.; Vulpio, A. Numerical analysis of particle deposition in an aircraft engine compressor cascade. In Proceedings of the ASME Turbo Expo 2020: Turbomachinery Technical Conference and Exposition, Virtual, 21–25 September 2020.